Article
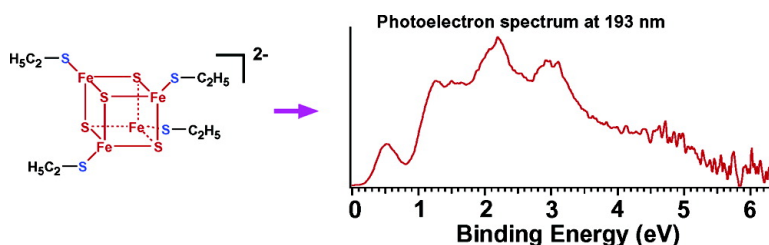
Probing the Intrinsic Electronic Structure of the Cubane [4Fe–4S] Cluster: Nature's Favorite Cluster for Electron Transfer and Storage

Xue-Bin Wang, Shuqiang Niu, Xin Yang, Saad K. Ibrahim,
Christopher J. Pickett, Toshiko Ichiye, and Lai-Sheng Wang

More About This Article

Additional resources and features associated with this article are available within the HTML version:

- Supporting Information
- Links to the 5 articles that cite this article, as of the time of this article download
- Access to high resolution figures
- Links to articles and content related to this article
- Copyright permission to reproduce figures and/or text from this article

View the Full Text HTML

Probing the Intrinsic Electronic Structure of the Cubane [4Fe−4S] Cluster: Nature's Favorite Cluster for Electron Transfer and Storage

Xue-Bin Wang,[†,‡] Shuqiang Niu,[§,||] Xin Yang,[‡] Saad K. Ibrahim,[⊥]
Christopher J. Pickett,[⊥] Toshiko Ichiye,[§,||] and Lai-Sheng Wang*,[†,‡]

*W. R. Wiley Environmental Molecular Sciences Laboratory, Pacific Northwest National
Laboratory, P.O. Box 999, Richland, Washington 99352, Department of Physics,
Washington State University, 2710 University Drive, Richland, Washington 99352,
School of Molecular Biosciences, Washington State University, Pullman, Washington 99164,
Department of Chemistry, Georgetown University, Washington, D.C. 20057-1227, and
Department of Biological Chemistry, John Innes Centre, Norwich, NR4 7UH, United Kingdom*

Received June 23, 2003; E-mail: ls.wang@pnl.gov

Abstract: The cubane [4Fe−4S] is the most common multinuclear metal center in nature for electron transfer and storage. Using electrospray, we produced a series of gaseous doubly charged cubane-type complexes, $[Fe_4S_4L_4]^{2-}$ (L = −SC_2H_5, −SH, −Cl, −Br, −I) and the Se-analogues $[Fe_4Se_4L_4]^{2-}$ (L = −SC_2H_5, −Cl), and probed their electronic structures with photoelectron spectroscopy and density functional calculations. The photoelectron spectral features are similar among all the seven species investigated, revealing a weak threshold feature due to the minority spins on the Fe centers and confirming the low-spin two-layer model for the $[4Fe−4S]^{2+}$ core and its "inverted level scheme". The measured adiabatic detachment energies, which are sensitive to the terminal ligand substitution, provide the intrinsic oxidation potentials of the $[Fe_4S_4L_4]^{2-}$ complexes. The calculations revealed a simple correlation between the electron donor property of the terminal thiolate as well as the bridging sulfide with the variation of the intrinsic redox potentials. Our data provide intrinsic electronic structure information of the [4Fe−4S] cluster and the molecular basis for understanding the protein and solvent effects on the redox properties of the [4Fe−4S] active sites.

Introduction

Cluster science is a relatively nascent research field that promises a molecular-level understanding of catalysis and discovery of new nanomaterials.[1] However, nature has been utilizing clusters from the beginning of life. Among the important clusters in biochemistry are the Fe−S clusters,[2] which constitute the active sites of a growing list of proteins in such essential life-sustaining processes as respiration, nitrogen fixation, and photosynthesis.[3−5] The most prototypical and ubiquitous Fe−S cluster is the cubane-type [4Fe−4S] cluster, which, in addition to its catalytic and regulatory roles, appears to be nature's most favorite agent for electron transfer and storage,[2] such as in ferredoxins (Fds),[6] high potential proteins (HiPIPs),[7] and the integral machineries of hydrogenases and nitrogenases.[8,9]

In proteins, the cubane [4Fe−4S] unit is usually coordinated by the amino acid cysteine (Figure 1). The [4Fe−4S] core functions as electron transfer agent usually between the following oxidation states, $[4Fe−4S]^{1+} \leftrightarrow [4Fe−4S]^{2+} \leftrightarrow [4Fe−4S]^{3+}$. A fourth state, the all-ferrous species $[4Fe−4S]^0$, was also detected in the iron protein of nitrogenase.[10−13]

It is important to understand the intrinsic electronic structure of the Fe−S clusters and modifications by their surroundings in order to understand the properties and functionalities of the iron−sulfur proteins. Various spectroscopic techniques and theoretical methods have been used to interrogate the magnetic and electronic structures of the Fe−S clusters in both synthetic analogues and proteins.[2,14−24] Extensive theoretical works using

† W. R. Wiley Environmental Molecular Sciences Laboratory, Pacific Northwest National Laboratory.
‡ Department of Physics, Washington State University.
§ School of Molecular Biosciences, Washington State University.
|| Department of Chemistry, Georgetown University.
⊥ Department of Biological Chemistry, John Innes Centre.

(1) Wang, L. S. Clusters. In *Encyclopedia of Chemical Physics and Physical Chemistry*; Moore, J. H., Spencer, N. D., Eds.; IOP Publishing: Philadelphia, 2001; Vol. III, pp 2113−2130.
(2) Beinert, H.; Holm, R. H.; Münck, E. *Science* **1997**, *277*, 653.
(3) Lovenberg, W. Ed. *Iron−Sulfur Proteins*; Academic Press: New York, 1973; Vols. I and II.
(4) Spiro, T. G. Ed. *Iron−Sulfur Proteins*; Wiley-Interscience: New York, 1982.
(5) Cammack, R. *Adv. Inorg. Chem.* **1992**, *38*, 281.
(6) Dauter, Z.; Wilson, K. S.; Sieker, L. C.; Meyer, J.; Moulis, J. M. *Biochemistry* **1997**, *36*, 16 065.
(7) Kerfeld, C. A.; Salmeen, A. E.; Yeates, T. O. *Biochemistry* **1998**, *37*, 13 911.
(8) Peters, J. W.; Lanzilotta, W. N.; Lemon, B. J.; Seefeldt, L. C. *Science* **1998**, *282*, 1853.
(9) Einsle, O.; Tezcan, F. A.; Andrade, S. L. A.; Schmid, B.; Yoshida, M.; Howard, J. B.; Rees, D. C. *Science* **2002**, *297*, 1696.
(10) Watt, G. D.; Reddy, K. R. N. *J. Inorg. Biochem.* **1994**, *53*, 281.
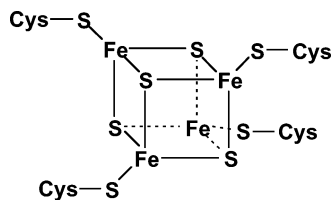(11) Angove, H. C.; Yoo, S. J.; Burgess, B. K.; Münck, E. *J. Am. Chem. Soc.* **1997**, *119*, 8730.
(12) Musgrave, K. B.; Angove, H. C.; Burgess, B. K. Hedman, B. Hodgson, K. O. *J. Am. Chem. Soc.* **1998**, *120*, 5325.
(13) Yoo. S. J.; Angove, H. C.; Burgess, B. K.; Hendrich, M. P.; Münck, E. *J. Am. Chem. Soc.* **1999**, *121*, 2534.
(14) Ibers, J. A.; Holm, R. H. *Science* **1980**, *209*, 223.
(15) Holm, R. H.; Ibers, J. A. *Iron−Sulfur Proteins III*; Lovenberg, W., Ed.; Academic Press: New York, 1977; p 205.

Figure 1. Schematic structure of the [4Fe−4S] active site in proteins.

broken-symmetry density functional theory[21−24] have shown that the [4Fe−4S]$^{2+}$ core can be viewed as a two-layer system, where two high-spin Fe in each [2Fe−2S] sublayer are coupled ferromagnetically, and the two [2Fe−2S] sublayers are coupled antiferromagnetically to give a low-spin state. The theoretical results are consistent with experimental observations from Mössbauer and EPR spectroscopy.[2]

The reduction potential is one of the most important functional characteristics for an electron-transfer protein. For the [4Fe−4S] core, the redox couple in Fds involves [Fe$_4$S$_4$(S$_{Cys}$)$_4$]$^{2−}$/[Fe$_4$S$_4$(S$_{Cys}$)$_4$]$^{3−}$ with reduction potentials ranging from −645 to 0 mV. The redox couple in HiPIP involves [Fe$_4$S$_4$(S$_{Cys}$)$_4$]$^{1−}$/[Fe$_4$S$_4$(S$_{Cys}$)$_4$]$^{2−}$ with reduction potentials ranging from 50 to 450 mV; the [Fe$_4$S$_4$(S$_{Cys}$)$_4$]$^{2−}$/[Fe$_4$S$_4$(S$_{Cys}$)$_4$]$^{3−}$ redox couple in HiPIP was estimated to lie near −1000 mV.[25,26] Because the free energy of a reduction reaction can be divided into the intrinsic free energy of the prosthetic group, the [4Fe−4S] core, and the extrinsic free energy due to the protein surrounding and the solvent at the redox site ($\Delta G° = \Delta G_{int} + \Delta G_{env} + \Delta G_{int/env}$),[27] identifying the intrinsic and environmental determinants that lead to this large range in reduction potentials is crucial in understanding the functions of the Fe−S proteins. Major environmental factors contributing to the reduction potentials of Fe−S proteins have been suggested to include the H-bonding to the cysteine and bridging sulfide ligands, dipole interactions with the Fe−S cluster from the solvent and the protein side-chain/backbone, and electrostatic interactions.[28−30] For instance, the larger number of NH···S H-bonds to the redox site in the Fds than in the HiPIPs, as well as the more solvent-exposed redox sites in the Fds, was suggested to be responsible for the differences in their reduction potentials. Alteration of the reduction potentials of the [4Fe−4S]$^{2+}$/[4Fe−4S]$^{1+}$ couple have been reported by changing the cluster environment.[31,32] Theoretical calculations of the reduction potentials of the [4Fe−4S] cluster were also carried out, in which environmental effects were evaluated using a continuum dielectric model.[33,34] However, the environmental effects on the electronic structure and redox properties of the [4Fe−4S] core remain uncertain.

Gas-phase photodetachment photoelectron spectroscopy (PES) is a powerful experimental technique to study the electronic structure and chemical bonding of isolated molecules without perturbation of the solvents or crystal field or the protein environment, yielding the intrinsic properties of the Fe−S clusters and providing the basis for elucidating the complex cluster-protein interactions. Photodetachment, involving removal of an electron from a molecule (AB$^{n−}$ → AB$^{(n−1)}$ + e$^−$), is an oxidation process. The measured adiabatic electron detachment energy (ADE) reflects the energy difference between the oxidized and reduced species in the gas phase, providing the intrinsic reduction potential,[35] $\Delta G_{int} \approx \Delta E_{int} = -ADE = -(VDE + \lambda_{oxd})$, where VDE represents the vertical electron detachment energy and λ_{oxd} represent the oxidation reorganization energy. We have developed an experimental technique, which couples an electrospray ionization (ESI) source with a magnetic-bottle photoelectron spectrometer.[36] ESI is a versatile technique, allowing ionic species in solution samples to be transported into the gas phase. Our research has shown that the new ESI-PES technique is ideal for investigating multiply charged anions in the gas-phase,[37] as well as anionic metal-complexes commonly present in solution.[35,38−43] Using this technique, we have reported systematic PES and theoretical studies on a series of [1Fe] Fe−S complex anions, which are analogues of the redox site in rubredoxin[35,42,43] and Fe(I)−Fe(I) model complexes for the di-iron subsite of the [Fe]-hydrogenase.[44] Very recently, we observed symmetric fission in a series of doubly charged gaseous cubane complexes, [Fe$_4$S$_4$X$_4$]$^{2−}$ → 2[Fe$_2$S$_2$X$_2$]$^−$ (X = Cl, Br, SC$_2$H$_5$).[45,46]

Here, we report a comprehensive investigation of the intrinsic electronic structure of a series of free cubane [4Fe−4S] complexes, [Fe$_4$S$_4$L$_4$]$^{2−}$ (L = SH, SC$_2$H$_5$, Cl, Br, I) and the Se-substituted [Fe$_4$Se$_4$L$_4$]$^{2−}$ (L = Cl, SC$_2$H$_5$) species using PES and density functional theory (DFT) calculations. PES spectra were taken at five different photon energies: 532, 355, 266, 193, and 157 nm. The photon energy dependent studies allowed us to probe the intramolecular Coulomb repulsion and the repulsive Coulomb barrier (RCB) in these doubly charged anions.[37] The influences of both the terminal ligands and the bridging ligands

(16) Bertini, I.; Ciurli, S.; Luchinat, C. *Struct. Bonding (Berlin)* **1995**, *83*, 1.
(17) Holm, R. H.; Kennepohl, P.; Solomon, E. I. *Chem. Rev.* **1996**, *96*, 2239.
(18) Glaser, T.; Hedman, B.; Hodgson, K. O.; Solomon, E. I. *Acc. Chem. Res.* **2000**, *33*, 859.
(19) Glaser, T.; Rose, K.; Shadle, S. E.; Hedman, B.; Hodgson, K. O.; Solomon, E. I. *J. Am. Chem. Soc.* **2001**, *123*, 442.
(20) Glaser, T.; Bertini, I.; Moura, J. J. G.; Hedman, B.; Hodgson, K. O.; Solomon, E. I. *J. Am. Chem. Soc.* **2001**, 123, 4859.
(21) Aizman, A.; Case, D. A. *J. Am. Chem. Soc.* **1982**, *104*, 3269.
(22) Noodleman, L.; Baerends, E. J. *J. Am. Chem. Soc.* **1984**, *106*, 2316.
(23) Noodleman, L.; Case, D. A. *Ad. Inorg. Chem.* **1992**, *38*, 423.
(24) Noodleman, L.; Peng, C. Y.; Case, D. A.; Mouesca, J.-M. *Coord. Chem. Rev.* **1995**, *144*, 199.
(25) Cammack, R. Iron−Sulfur Cluster in Enzymes: Themes and Variations. In *Iron−Sulfur Proteins*; Cammack, R., Ed.; Academic Press: San Diego, 1992; p 281.
(26) Stephens, P. J.; Jollie, D. R.; Warshel, A. *Chem. Rev.* **1996**, *96*, 2491.
(27) Ichiye, T. Computational Studies of Redox Potentials of Electron-Transfer Proteins. In *Simulation and Theory of Electrostatic Interactions in Solution*; Pratt, L. R., Hummer, G., Eds.; American Institute of Physics: Woodbury, NY, 1999; p 431.
(28) Adman, E. T.; Watenpaugh, K. D.; Jensen, L. H. *Pro. Natl. Acad. Sci. U.S.A.* **1975**, *72*, 4854.
(29) Backes, G.; Mino, Y.; Loehr, T. M.; Meyer, T. E.; Cusanovich, M. A.; Sweeney, W. V.; Adman, E. T.; Sanders-Loehr, J. *J. Am. Chem. Soc.* **1991**, *113*, 2055.
(30) Pickett, C. J.; Ryder, K. S. *J. Chem. Soc., Dalton Trans.* **1994**, 2181.

(31) Chen, K.; Tilley, G. J.; Sridhar, V.; Prasad, G. S.; Stout, C. D.; Armstrong, F. A.; Burgess, B. K. *J. Biol. Chem*. **1999**, 274, 36 479.
(32) Zhou, C.; Raebiger, J. W.; Segal, B. M.; Holm, R. H. *Inorg. Chim. Acta* **2000**, *300−302*, 892.
(33) Mouesca, J.-M.; Chen, J. L.; Noodleman, L.; Bashford, D.; Case, D. A. *J. Am. Chem. Soc*. **1994**, *116*, 11 898.
(34) Torres, R. A.; Lovell, T.; Noodleman, L.; Case, D. A. *J. Am. Chem. Soc.* **2003**, *125*, 1923.
(35) Wang, X. B.; Wang, L. S. *J. Chem. Phys.* **2000**, *112*, 6959.
(36) Wang, L. S.; Ding, C. F.; Wang, X. B.; Barlow, S. E. *Rev. Sci. Instrum.* **1999**, *70*, 1957.
(37) Wang, L. S.; Wang, X. B. *J. Phys. Chem. A* **2000**, *104*, 1978.
(38) Wang, X. B.; Wang, L. S.; Brown, R.; Schwerdtfeger, P.; Schröder, D.; Schwarz, H. *J. Chem. Phys.* **2001**, *114*, 7388.
(39) Wang, X. B.; Wang, L. S. *J. Phys. Chem. A* **2000**, *104*, 4429.
(40) Wang, X. B.; Wang, L. S. *J. Am. Chem. Soc.* **2000**, *122*, 2339.
(41) Wang, X. B.; Wang, L. S. *J. Am. Chem. Soc.* **2000**, *122*, 2096.
(42) Yang, X.; Wang, X. B.; Fu, Y. J. Wang, L. S. *J. Phys. Chem. A* **2003**, *107*, 1703.
(43) Niu, S. Q.; Wang, X. B.; Nichols, J. A.; Wang, L. S.; Ichiye, T. *J. Phys. Chem. A* **2003**, *107*, 2898.
(44) Yang, X.; Razavet, M.; Wang, X. B.; Pichett, C. J.; Wang, L. S. *J. Phys. Chem. A* **2003**, *107*, 4612.
(45) Yang, X.; Wang, X. B.; Niu, S. Q.; Pickett, C. J.; Ichiye, T.; Wang, L. S. *Phys. Rev. Lett.* **2002**, *89*, 16 340−16 341.
(46) Niu, S. Q.; Wang, X. B.; Yang, X.; Wang, L. S.; Ichiye, T., submitted.

(substitution of S by Se) on the electronic structure of the cubane core are investigated. Similar spectral features are observed for all the cubane complexes, revealing their similar electronic structure and the robustness of the [4Fe−4S] core as a modular unit. The spectral features confirm the low-spin two-layer model for the [4Fe−4S]$^{2+}$ core and its "inverted level scheme". The measured ADEs provide the intrinsic oxidation energies of the [Fe$_4$S$_4$L$_4$]$^{2-}$ complexes. We found the ADEs of [Fe$_4$S$_4$X$_4$]$^{2-}$ are very sensitive to the types of the terminal ligands, whereas very little change in ADE was observed upon substitution of the inorganic (bridging) S by Se. DFT calculations showed that the major factor contributing to these changes is due to the electron donor property of the terminal ligands, which destabilize the electron to be oxidized from the singly occupied $\sigma^*_{\text{Fe−S}}$ molecular orbital (MO) of [Fe$_4$S$_4$(SR)$_4$]$^{2-}$. The major factor influencing the reduction energy of [Fe$_4$S$_4$(SR)$_4$]$^{2-}$ is found to be the donor property of the bridging S. Our data provide intrinsic electronic structure information of the cubane [4Fe−4S] core and the molecular basis for understanding the protein and solvent effects on the properties of the [4Fe−4S] active sites.

Experimental Methods

The experiment was carried out using an experimental apparatus equipped with a magnetic-bottle time-of-flight photoelectron analyzer and an ESI source. Details of the experimental method have been given elsewhere.[36] Briefly, the anions of interest, [Fe$_4$S$_4$L$_4$]$^{2-}$ (L = −SC$_2$H$_5$, −SH, −Cl, −Br, −I) and [Fe$_4$Se$_4$L$_4$]$^{2-}$ (L = −SC$_2$H$_5$, −Cl), were produced from electrospray of 10^{-3} M solutions of their corresponding tetrabutylammonium salts in O$_2$-free acetonitrile. Anions produced from the ESI source were guided into a quadruple ion-trap, where ions were accumulated for 0.1 s before being pulsed into the extraction zone of a time-of-flight mass spectrometer.

During the PES experiment, the [Fe$_4$S$_4$L$_4$]$^{2-}$ or [Fe$_4$Se$_4$L$_4$]$^{2-}$ species were mass-selected and decelerated before being intercepted by a probe laser beam in the photodetachment zone of the magnetic-bottle photoelectron analyzer. In the current study, we employed five detachment photon energies, 532 nm (2.331 eV), 355 nm (3.496 eV), and 266 nm (4.661 eV) from a Nd:YAG laser, and 193 nm (6.424 eV) and 157 nm (7.866 eV) from an excimer laser. All experiments were performed at 20 Hz repetition rate with the ion beam off at alternating laser shots for background subtraction, which was critical for high photon energy experiments (>4.661 eV) due to background noises. Photoelectrons were collected at nearly 100% efficiency by the magnetic-bottle and analyzed in a 4-meter long electron flight tube. Photoelectron time-of-flight spectra were collected and then converted to kinetic energy spectra, calibrated by the known spectra of I$^-$ and O$^-$. The electron binding energy spectra presented here were obtained by subtracting the kinetic energy spectra from the detachment photon energies. The energy resolution ($\Delta E/E$) was about 2%, i.e., ~10 meV for 0.5 eV electrons, as measured from the spectrum of I$^-$ at 355 nm.

Theoretical Methods

The broken-symmetry DFT method,[47] specifically with the Becke's three-parameter hybrid exchange functional[48−50] and the Lee−Yang−Parr correlation functional (B3LYP)[51] using two different basis sets, 6-31G** and 6−31(++)G**,[52−54] was utilized for the geometry optimizations, electronic structure, and energy calculations of the [Fe$_4$S$_4$L$_4$]$^{3-}$/[Fe$_4$S$_4$L$_4$]$^{2-}$/[Fe$_4$S$_4$L$_4$]$^{1-}$ (L = SCH$_3$, SH, Cl) and [Fe$_4$Se$_4$-(SCH$_3$)$_4$]$^{2-}$/[Fe$_4$Se$_4$(SCH$_3$)$_4$]$^{1-}$ redox couples. We used the simpler −SCH$_3$ ligand in all the calculations, instead of the more complex −SC$_2$H$_5$ ligand, which does not significantly change the electronic properties of the complexes. No symmetry constraints were imposed during geometry optimizations, and each structure was confirmed to be a ground-state structure by several separate calculations on different possible configuration states. This procedure is necessary because the electronic structure is very sensitive to the iron−sulfur cluster structure. The calculated energies were refined at the B3LYP/6−31(++)$_s$G**//B3LYP/6-31G** level, where sp-type diffuse functions were added to the 6-31G** basis set of the sulfur and chlorine atoms,[52−57] which significantly improved the accuracy of the calculated oxidation potentials of the iron−sulfur redox couples.[43] Because of the doubly charged nature of the cubane complexes, the addition of the diffuse functions is important. The ADE of [Fe$_4$S$_4$L$_4$]$^{2-}$ was calculated as the total energy difference between the ground states of [Fe$_4$S$_4$L$_4$]$^{2-}$ and [Fe$_4$S$_4$L$_4$]$^-$; the VDE was calculated as the energy difference between the ground state of [Fe$_4$S$_4$L$_4$]$^{2-}$ and the energy of [Fe$_4$S$_4$L$_4$]$^-$ at the geometry of [Fe$_4$S$_4$L$_4$]$^{2-}$. All calculations were performed using the NWChem program package.[58] The molecular orbital visualizations were performed using the extensible computational chemistry environment (Ecce) application software.[59]
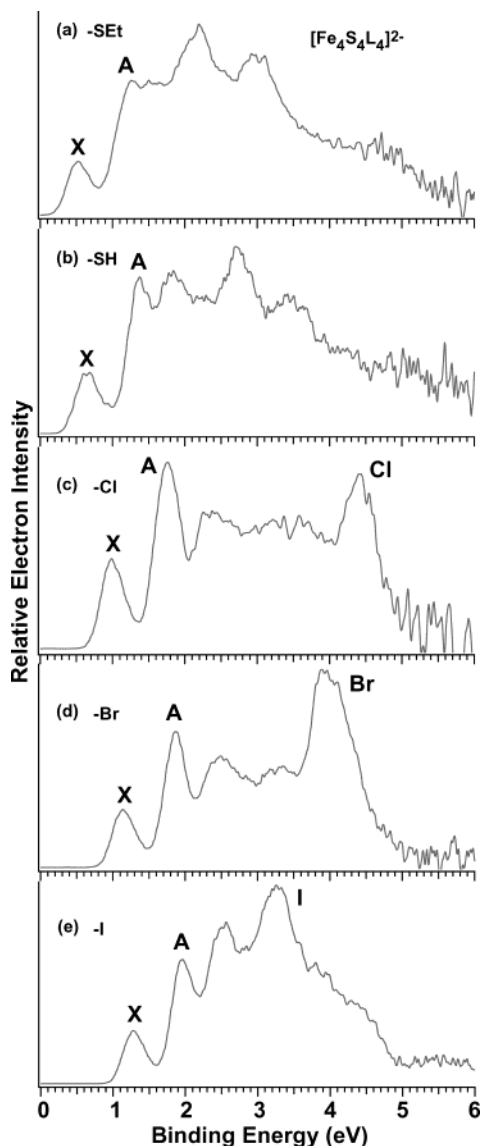
Experimental Results

Photoelectron Spectra of the [Fe$_4$S$_4$L$_4$]$^{2-}$ Complexes at 193 nm. The 193-nm spectra of [Fe$_4$S$_4$L$_4$]$^{2-}$ (L = SC$_2$H$_5$, SH, Cl, Br, I) are shown in Figure 2. The spectral patterns of all the data show certain similarities. A weak but well-defined threshold feature X was observed in the spectra of all the samples. A second band A, well separated from the threshold band, was not well resolved in the spectrum of [Fe$_4$S$_4$(SC$_2$H$_5$)$_4$]$^{2-}$ (Figure 2a), but became a well-defined peak in the spectra of [Fe$_4$S$_4$(SH)$_4$]$^{2-}$ and the halide complexes. The relative intensities of the bands X and A, their bandwidths, as well as the X−A energy gap (∼0.75 eV), are almost identical in all the spectra. High binding energy features in the spectra exhibit differences due to the different terminal ligands. A prominent feature emerges in the spectrum of [Fe$_4$S$_4$Cl$_4$]$^{2-}$ at ∼4.4 eV. It shifts to lower binding energies in the spectra of the bromide and iodide complexes and is easily recognized as the halogen ligand feature (Figure 2c−e). The spectra of the SC$_2$H$_5$ and the SH complexes are nearly identical, except that the broad feature at the very high binding energy side (∼5 eV) appeared to be more intense in the spectrum of SC$_2$H$_5$ (Figure 2a), reflecting the contribution from the C$_2$H$_5$ groups. In addition to the prominent halide features, the major difference between the spectra of the halide complexes and those of the SC$_2$H$_5$ and SH complexes is in the spectral range above the A band. The overall spectral intensities in these spectral range are higher in the spectra of the SC$_2$H$_5$ and SH complexes, reflecting the contribution from the terminal ligand S. Despite the overall similarities of spectral patterns among the five complexes, their electron binding energies were observed to depend on the type of ligands, increasing in the direction SC$_2$H$_5$ → SH → Cl → Br → I.

(47) Parr, R. G.; Yang, W. *Density-Functional Theory of Atoms and Molecules*; Oxford University Press: Oxford, 1989.
(48) Becke, A. D. *Phys. Rev.* **1988**, *A38*, 3098.
(49) Becke, A. D. *J. Chem. Phys.* **1993**, *98*, 1372.
(50) Becke, A. D. *J. Chem. Phys.* **1993**, *98*, 5648.
(51) Lee, C.; Yang, W.; Parr, R. G. *Phys. Rev.* **1988**, *B37*, 785.
(52) Rassolov, V.; Pople, J. A.; Ratner, M.; Windus, T. L. *J. Chem. Phys.* **1998**, *109*, 1223.

(53) Francl, M. M.; Petro, W. J.; Hehre, W. J.; Binkley, J. S.; Gordon, M. S.; DeFrees, D. J.; Pople, J. A. *J. Chem. Phys.* **1982**, *77*, 3654.
(54) Hariharan, P. C.; Pople, J. A. *Theor. Chimica Acta* **1973**, *28*, 213.
(55) Clark, T.; Chandrasekhar, J.; Schleyer, P. v. R. *J. Comput. Chem.* **1983**, *4*, 294.
(56) Krishnam, R.; Binkley, J. S.; Seeger, R.; Pople, J. A. *J. Chem. Phys.* **1980**, *72*, 650.
(57) Gill, P. M. W.; Johnson, B. G.; Pople J. A.; Frisch, M. J. *Chem. Phys. Lett.* **1992**, *197*, 499.
(58) High Performance Computational Chemistry Group, *NWChem, A Computational Chemistry Package for Parallel Computers, Version 4.5*; Pacific Northwest National Laboratory, Richland, WA 99352, USA, 2003.
(59) Black, G.; Chase, J.; Didier, B.; Feller, D.; Gracio, D.; Jones, D.; Jurrus, E.; Keller, T.; Matsumoto, S.; Mendoza, E.; Nordwall, D.; Olander, M.; Palmer, B.; Peden, N.; Schuchardt, K.; Stephan, E.; Taylor, H.; Thomas, G.; Vorpagel, E.; Windus, T.; *Ecce, A Problem Solving Environment for Computational Chemistry, Software Version 1.5*; Pacific Northwest National Laboratory, Richland, WA 99352-0999, USA, 2000.

Figure 2. Photoelectron spectra of (a) $[Fe_4S_4(SC_2H_5)_4]^{2-}$, (b) $[Fe_4S_4(SH)_4]^{2-}$, (c) $[Fe_4S_4Cl_4]^{2-}$, (d) $[Fe_4S_4Br_4]^{2-}$, and (e) $[Fe_4S_4I_4]^{2-}$ at 193 nm.

Photoelectron Spectra of the $[Fe_4Se_4L_4]^{2-}$ Complexes at 193 nm. The spectra of the Se-substituted $[Fe_4Se_4L_4]^{2-}$ (X = SC_2H_5, Cl) are shown in Figure 3 along with a comparison with the corresponding $[Fe_4S_4L_4]^{2-}$ anions. It seems that the substitution of the bridging S by Se has little effect on the PES spectra, i.e., the electronic structure of the cubane core. Both the spectral patterns and the electron binding energies of the two $[Fe_4Se_4L_4]^{2-}$ species are almost identical to those of their $[Fe_4S_4L_4]^{2-}$ counterparts except the slight change of the relative intensities of band *X* and *A* and the energy gap between them. The *A* band is relatively stronger in the spectra of the Se-bridged complexes. The *X*−*A* energy gaps of $[Fe_4Se_4(SC_2H_5)_4]^{2-}$ and $[Fe_4Se_4Cl_4]^{2-}$ are the same (∼0.69 eV), which is slightly smaller than those observed for the $[Fe_4S_4L_4]^{2-}$ species (∼0.75 eV).

Photoelectron Spectra at Various Photon Energies. The photon-energy-dependent PES spectra of all the seven dianions are shown in Figures 4−10, respectively. PES spectra of $[Fe_4S_4L_4]^{2-}$ (L = SC_2H_5, SH) and $[Fe_4Se_4(SC_2H_5)_4]^{2-}$ were taken at all the five photon energies, whereas only 355, 266, 193, and 157 nm spectra were taken for the four complexes with halide ligands due to their higher electron binding energies. In the lower photon energy spectra, high binding energy features observed in higher photon energy spectra disappeared as a direct consequence of the RCB in multiply charged anions.[37] From these data,
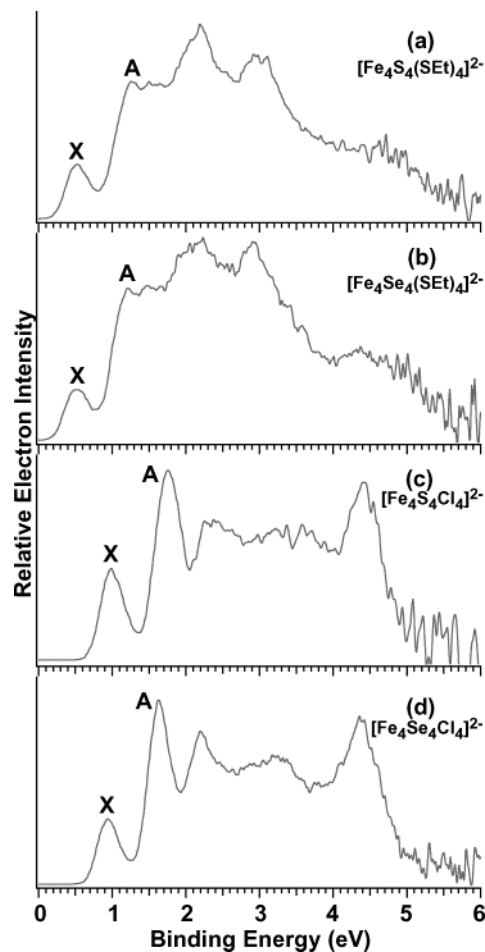

Figure 3. Comparison of the 193 nm photoelectron spectra between (a) $[Fe_4S_4(SC_2H_5)_4]^{2-}$ and (b) $[Fe_4Se_4(SC_2H_5)_4]^{2-}$, (c) $[Fe_4S_4Cl_4]^{2-}$ and (d) $[Fe_4Se_4Cl_4]^{2-}$.

the barrier height for each dianion can be estimated, as discussed later. High binding energy sharp features in the 266 nm spectra in Figures 6−8 and the 355 nm spectrum in Figure 8 were due to the halide anions L$^-$ (L = Cl, Br, I) as a result of photodissociation of the parent dianions and subsequent photodetachment by a second photon.

ADEs and VDEs. The ADE and VDE of the threshold peak (*X*) in the spectrum of each complex are listed in Table 1. Due to the lack of vibrational resolution, the ADEs were measured by drawing a straight line along the leading edge of the threshold band and then adding a constant to the intersection with the binding energy axis to take into account the instrumental resolution at the given energy range. This procedure was rather approximate, but consistent data were obtained from the spectra taken at different photon energies. The ADEs reported in Table 1 were determined from the lowest photon energy spectrum (532 or 355 nm) for each complex because of the better resolution at the lower photon energies. The VDE was measured straightforwardly from the peak maximum.
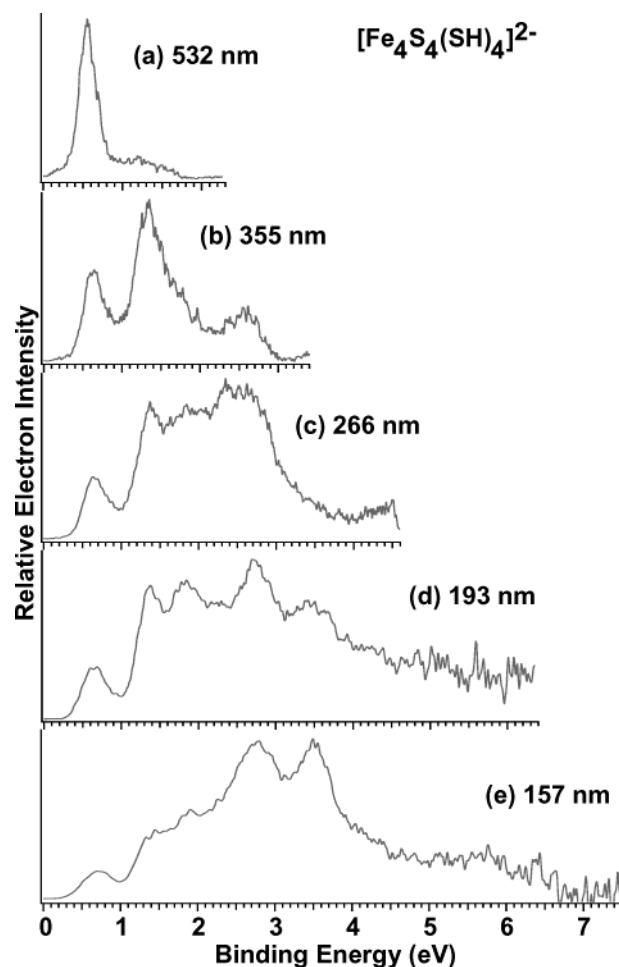
Theoretical Results

Generally, the cubane [4Fe−4S] redox site can be regarded as the coupling of two [2Fe−2S] redox layers according to broken symmetry DFT calculations.[21−24] One possibility for the coupling of the two layers is a high-spin ferromagnetically coupled state, in which the spins of the $[Fe_4S_4(SR)_4]^{2-}$ site are all aligned in a parallel manner in the two redox layers with twenty Fe 3d α electrons $(d_{Fe-Fe})^{\alpha}$ and two Fe 3d β electron $(d_{Fe-Fe})^{\beta}$, resulting in a high spin state (*S* = 18/2). Another
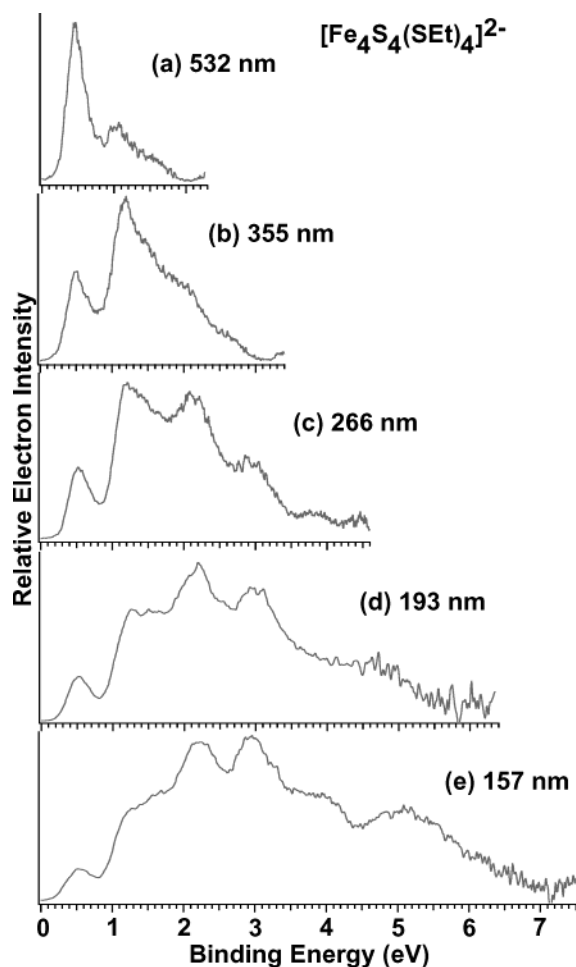
Figure 4. Photoelectron spectra of $[Fe_4S_4(SC_2H_5)_4]^{2-}$ at (a) 532 nm (2.331 eV), (b) 355 nm (3.496 eV), (c) 266 nm (4.661 eV), (d) 193 nm (6.424 eV), and (e) 157 nm (7.866 eV).

Figure 5. Photoelectron spectra of $[Fe_4S_4(SH)_4]^{2-}$ at (a) 532, (b) 355, (c) 266, (d) 193, and (e) 157 nm.

possibility is a low-spin state, in which the symmetry is broken because while each redox layer of the $[Fe_4S_4(SR)_4]^{2-}$ site couples ferromagnetically ($S = 9/2$), the spins of the two redox layers couple antiferromagnetically, giving rise to the low-spin state ($S = 0$). As shown schematically in Figure 11 for three oxidation levels of the [4Fe−4S] cubane, our DFT calculations showed that for $[Fe_4S_4(SCH_3)_4]^{3-/2-/1-}$ the low-spin state is favored by ∼0.7 eV relative to the high-spin state, which is in good agreement with the previous broken-symmetry DFT calculations[21−24] and experimental observations from Mössbauer and EPR spectroscopy.[2]

Our MO analysis showed that the spin-coupled interaction may split the MOs of the four individual iron sites in the uncoupled state into the Fe(3d) majority spin−orbitals and Fe(3d) minority spin−orbitals of the spin-coupled broken-symmetry state, $[Fe_4]^{10+}$, which interact with the MO's of the ligands, the terminal S(3p) and bridged S*(3p), to generate the higher-lying minority spin−orbitals and a set of lower-lying Fe(3d) majority spin−orbitals (Figure 12). On the basis of the broken-symmetry DFT calculations, the Fe(3d) majority spin states stabilized by ∼5−6 eV relative to the minority spin levels. The mainly ligand MOs are energetically situated between the minority and majority spin levels of Fe, giving rise to the so-called "inverted level scheme",[21−24] where the ligand levels are higher in energy than the Fe 3*d* levels (the majority spin levels),

as shown schematically in Figure 12a. The single valence-delocalized minority spin in each sublayer of $[Fe_2S_2]$ occupies the highest occupied molecular orbital (HOMO) of $[Fe_4S_4]^{2+}$ and this electron is transferred in an oxidation reaction or photodetachment of the $[Fe_4S_4L_4]^{2-}$ complexes.

Figure 13 shows the pictures of the HOMO and the lowest unoccupied molecular orbital (LUMO) from our calculations and the schematic MO diagrams. The HOMO of $[Fe_4S_4(SCH_3)_4]^{2-}$ (Figure 13b) exhibits a terminal Fe−S antibonding character, σ^*_{Fe-S}, with a strong bonding interaction between the two Fe on one sublayer. The LUMO (Figure 13a) shows a bridging Fe−S* antibonding character, σ^*_{Fe-S*}, with a strong antibonding interaction between the two Fe on one sublayer. When $[Fe_4S_4(SR)_4]^{2-}$ is oxidized to $[Fe_4S_4(SR)_4]^{1-}$, the process involves removing one electron from the HOMO σ^*_{Fe-S}. The sublayer on which this oxidation process occurs is called the "oxidized layer". When $[Fe_4S_4(SR)_4]^{2-}$ is reduced to $[Fe_4S_4(SR)_4]^{3-}$, one electron is added to the LUMO σ^*_{Fe-S*} on the "reduced layer", as schematically shown (Figures 11 and 13).

The B3LYP/6-31G** optimized geometries of $[Fe_4S_4(SCH_3)_4]^{3-/2-/1-}$ are given in Table 2 and compared with the X-ray crystal structures[60−62] of $[Fe_4S_4(SPh)_4]^{3-/2-/1-}$. It should be pointed out that the optimized geometries are for isolated
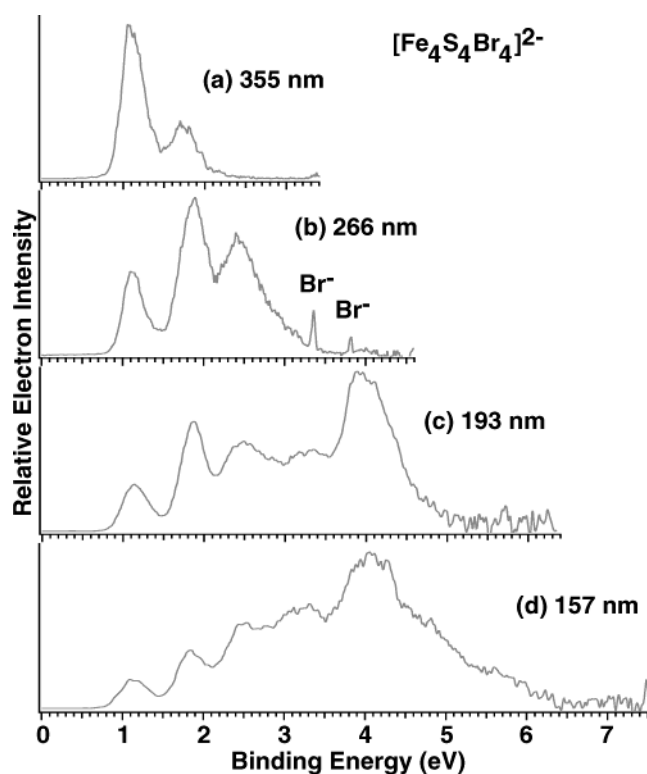
(60) Carney, M. J.; Papaefthymiou, G. C.; Whitener, M. A.; Spartalian, K.; Frankel, R. B.; Holm, R. H. *Inorg. Chem.* **1988**, *27*, 346.
(61) Excoffon, P.; Laugier, J.; Lamotte, B. *Inorg. Chem.* **1991**, *30*, 3075.
(62) O'Sullivan, T.; Millar, M. M. *J. Am. Chem. Soc.* **1985**, *107*, 4096.
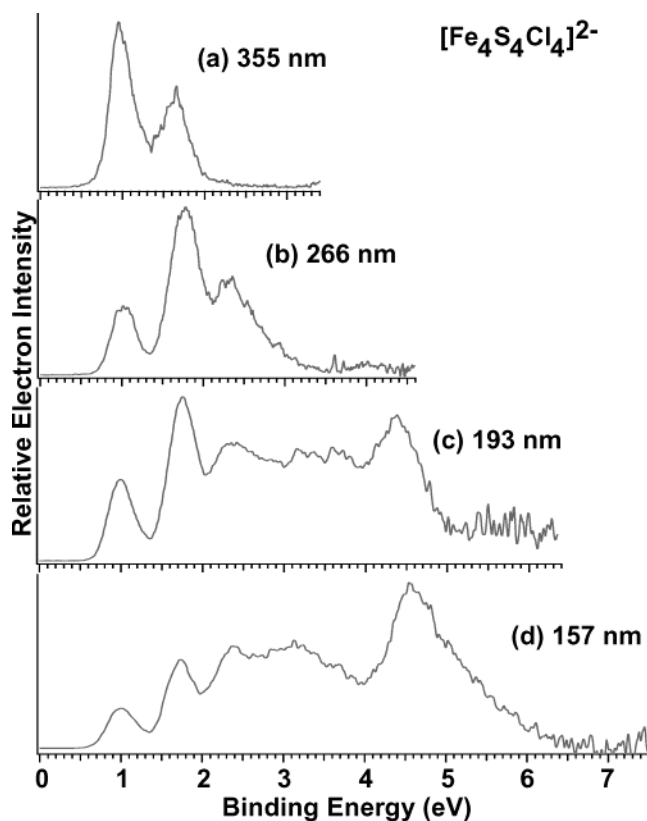
Figure 6. Photoelectron spectra of $[Fe_4S_4Cl_4]^{2-}$ at (a) 355, (b) 266, (c) 193, and (d) 157 nm.

Figure 7. Photoelectron spectra of $[Fe_4S_4Br_4]^{2-}$ at (a) 355, (b) 266, (c) 193, and (d) 157 nm.

complexes in the gas phase without counterions or the crystal environment. So the calculated Fe–Fe and Fe–S bond lengths tent to be larger than those determined from the X-ray crystal
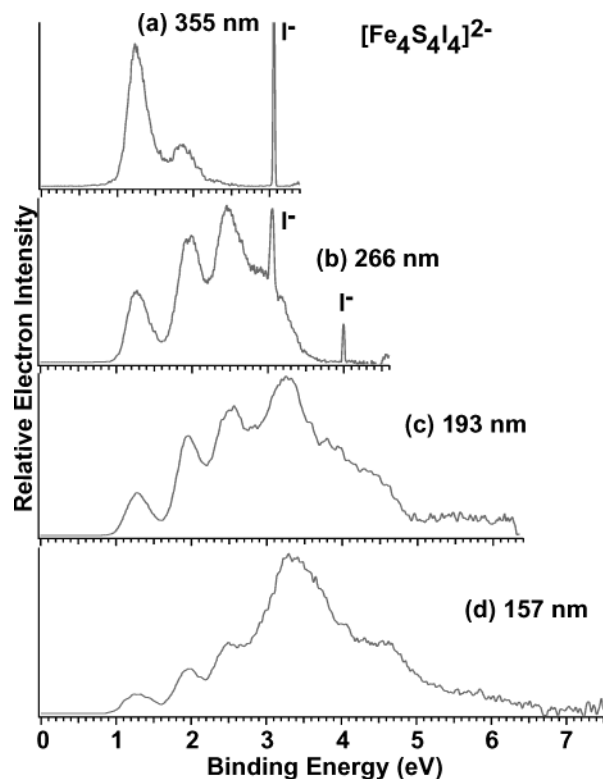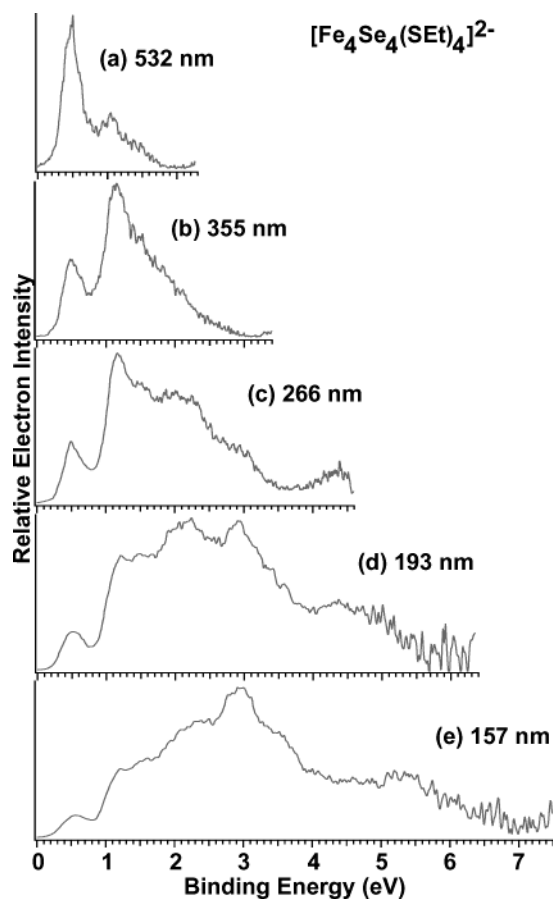

Figure 8. Photoelectron spectra of $[Fe_4S_4I_4]^{2-}$ at (a) 355, (b) 266, (c) 193, and (d) 157 nm.

structures. It is shown that from $[Fe_4S_4(SCH_3)_4]^{2-}$ to $[Fe_4S_4(SCH_3)_4]^{3-}$ both the Fe_{red}–Fe_{red} and the Fe_{red}–S^*_{red} distances in the reduced layer increase. From $[Fe_4S_4(SCH_3)_4]^{2-}$ to $[Fe_4S_4(SCH_3)_4]^{1-}$, Fe_{oxd}–Fe_{oxd} distance in the oxidized layer increases, but the Fe_{oxd}–S_{oxd} bond lengths decrease. We note that from $[Fe_4S_4(SR)_4]^{2-}$ to $[Fe_4S_4(SR)_4]^{3-}$ or $[Fe_4S_4(SR)_4]^{1-}$, the Fe–S* bond lengths within the reduced or oxidized layers tend to increase. The geometries of the reduced and oxidized sites determine these intrinsic electronic structures and pin the locations of the redox electrons. ADEs and VDEs of $[Fe_4S_4L_4]^{2-}$ ($L = SC_2H_5$, SH, Cl) and $[Fe_4Se_4(SC_2H_5)_4]^{2-}$ were calculated and compared with the experimental data (Table 1).
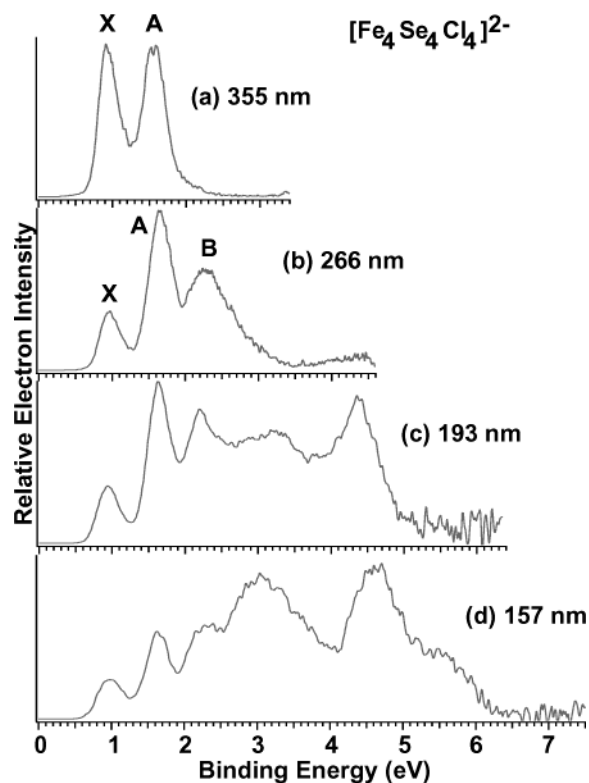
Discussion

The PES features shown in Figures 2–10 represent transitions from the ground state of the $[Fe_4S_4L_4]^{2-}$ or $[Fe_4Se_4L_4]^{2-}$ dianions to the ground and excited states of the corresponding singly charged anions. Within the single-particle approximation, the PES features can be viewed as removing electrons from the occupied MOs of the parent anions. Therefore, unlike other various experimental methods based on electronic transitions from occupied MOs to empty or partially occupied MOs, PES provides a direct map of the occupied MOs. Furthermore, for anions involved in electron transfer reactions, such as the [4Fe–4S] centers in Fds and HiPIPs, PES data directly yield the intrinsic oxidation energy and intramolecular reorganization energy in the gas phase.[35] In the following, we will first discuss the repulsive Coulomb barrier and the electrostatic interactions in these doubly charged anions. We will then discuss the PES data and the electronic structures of $[Fe_4S_4L_4]^{2-}$ in conjunction with the theoretical results. Finally, we will discuss the influences of the terminal and bridged ligands on the intrinsic redox potentials of $[Fe_4S_4L_4]^{2-/1-}$ couple.

Figure 9. Photoelectron spectra of $[Fe_4Se_4(SC_2H_5)_4]^{2-}$ at (a) 532, (b) 355, (c) 266, (d) 193, and (e) 157 nm.

Photon Energy Dependent Studies and the Repulsive Coulomb Barriers (RCB). One unique property of multiply charged anions is the existence of intramolecular Coulomb repulsion between the excess charges. When an electron is removed from a multiply charged anion (AB^{n-}), the two photoproducts ($AB^{(n-1)-} + e^-$) are both negatively charged. The superposition of the long-range Coulomb repulsion between the outgoing electron and the remaining anion and the short-range electron binding produces an effective potential barrier for the outgoing electron.[37,63–66] If the detachment photon energy is below the top of the RCB, then no electron detachment will occur even if the photon energy is above the asymptotic electron binding energy. In this case, detachment can only take place through electron tunneling, which depends exponentially on the distance between the photon energy and the RCB top and become negligible if the photon energy is far below the barrier top. When the photon energy is around the RCB top, the detachment signal may be reduced. In the tunneling regime, the appearance of the PES peak tends to shift to the lower binding energy side, due to a convolution of Franck–Condon factors and tunneling probabilities,[66] which depend on the electron kinetic energies exponentially. The intramolecular Coulomb repulsion and the resulting RCB have profound effects on the chemical and physical properties of multiply charged

(63) Wang, X. B.; Wang, L. S. *Nature* **1999**, *400*, 245.
(64) Wang, X. B.; Ding, C. F.; Wang, L. S. *Phys. Rev. Lett.* **1998**, *81*, 3351.
(65) Wang, L. S.; Ding, C. F.; Wang, X. B.; Nicholas, J. B. *Phys. Rev. Lett.* **1998**, *81*, 2667.
(66) Wang, X. B.; Ding, C. F.; Wang, L. S. *Chem. Phys. Lett.* **1999**, *307*, 391.

Figure 10. Photoelectron spectra of $[Fe_4Se_4Cl_4]^{2-}$ at (a) 355, (b) 266, (c) 193, and (d) 157 nm.

Table 1. Experimental Adiabatic (ADE), Vertical (VDE) Detachment Energies, Repulsive Coulomb Barriers (RCB), and Oxidation Reorganization Energies (λ_{oxd}) for $[Fe_4X_4L_4]^{2-}$ (X = S, Se; L = SC_2H_5, SH, Cl, Br, I)

| | ADE | | VDE | | | |
	exp.[a]	cal.	exp.[b]	cal.	RCB	λ_{oxd}
$[Fe_4S_4(SC_2H_5)_4]^{2-}$	0.29	0.16	0.52	0.47	1.6	0.23
$[Fe_4S_4(SH)_4]^{2-}$	0.39	0.41	0.63	0.80	1.5	0.24
$[Fe_4S_4Cl_4]^{2-}$	0.76	0.69	1.00	1.00	2.0	0.24
$[Fe_4S_4Br_4]^{2-}$	0.90		1.13		1.9	0.23
$[Fe_4S_4I_4]^{2-}$	1.06		1.28		1.8	0.22
$[Fe_4Se_4(SC_2H_5)_4]^{2-}$	0.28	0.16	0.51	0.39	1.6	0.23
$[Fe_4Se_4Cl_4]^{2-}$	0.72		0.94		2.0	0.22

[a] The estimated uncertainty for the ADEs is ±0.10 eV. [b] The estimated uncertainty for the VDEs is ±0.06 eV. Theoretical ADEs and VDEs for several complexes at B3LYP/6-31++G** level are shown for comparison. All energies are in eV.

anions. We have shown that the Coulomb repulsion is equal in magnitude to the RCB if the detached electron corresponds to the negative charge carrier or is localized on the charge carrier group.[65,67] In general, the RCB decreases with increasing physical sizes of the anions.

We have taken the PES spectra of $[Fe_4S_4L_4]^{2-}$ (L = SC_2H_5, SH) (Figures 4 and 5) and $[Fe_4Se_4(SC_2H_5)_4]^{2-}$ (Figure 9) at five different photon energies and $[Fe_4S_4L_4]^{2-}$ (L = Cl, Br, I) (Figures 6–8) and $[Fe_4Se_4Cl_4]^{2-}$ (Figure 10) at four photon energies, from which the height of the RCB can be estimated. The RCB effects on the PES data were seen most clearly in the photon-energy-dependent PES spectra, where the high binding energy features observed at high photon energies were severely cut off in the low photon energy spectra, as shown in Figures 4-10. On the basis of the spectral cutoff, the magnitude of the

(67) Wang, X. B.; Nicholas, J. B.; Wang, L. S. *J. Chem. Phys.* **2000**, *113*, 653.
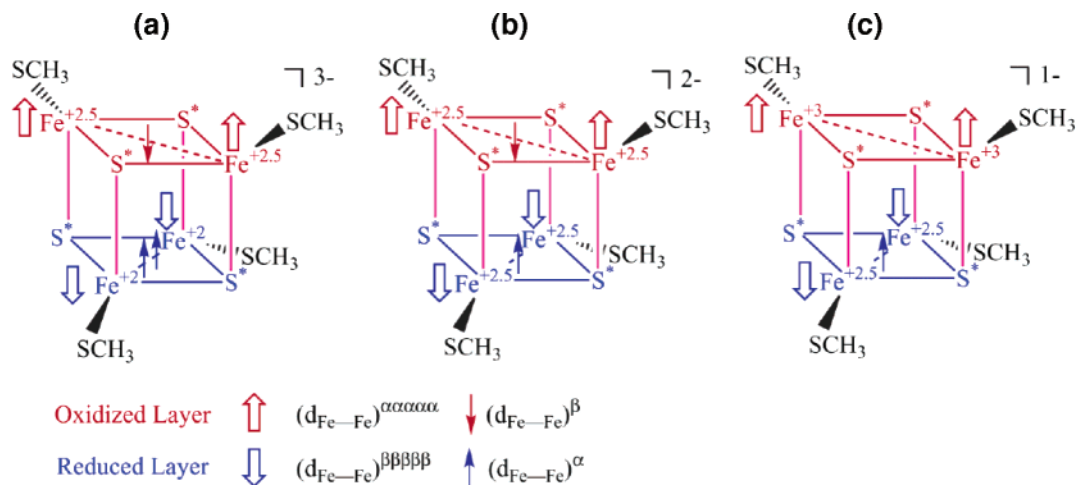
Figure 11. Schematic models of the spin couplings between the two redox sublayers of [4Fe−4S] cubane complexes at three different oxidation states, (a) 3−, (b) 2−, and (c) 1−. In each sublayer, the two high spin Fe centers couple ferromagnetically, while the two sublayers couple antiferromagnetically to give a low spin state. The 10 majority spins (represented by the large hollow arrows) are stabilized relative to the minority spin (represented by the small arrows), which is delocalized between the two Fe in each sublayer.
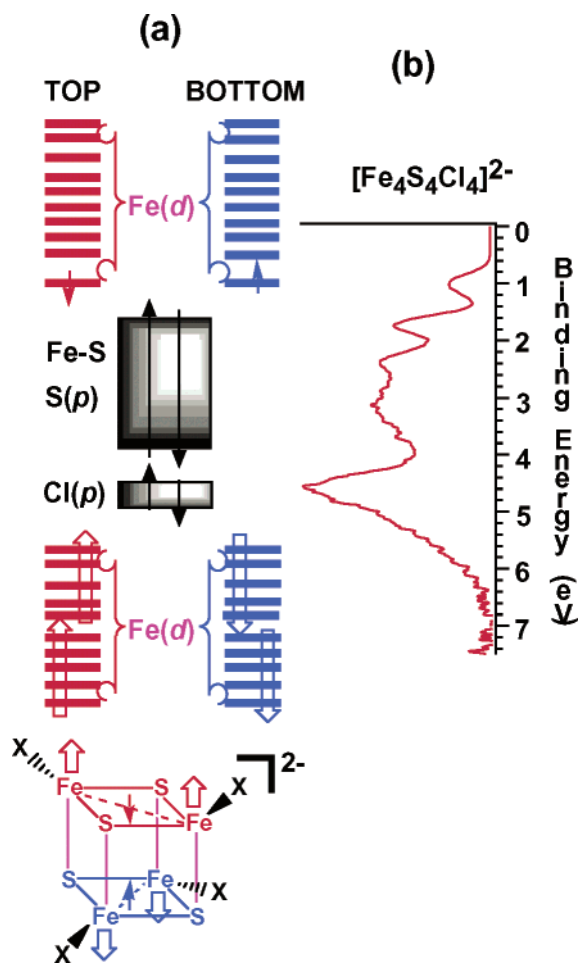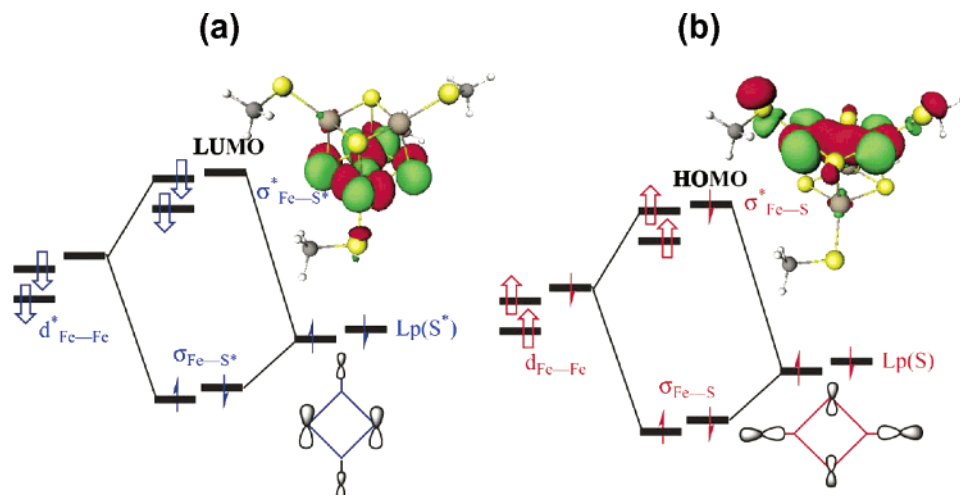

Figure 12. Schematic molecular orbital diagram showing the "inverted level scheme" and the spin coupling for the $[Fe_4S_4Cl_4]^{2-}$ cubane complex (a), in comparison with its photoelectron spectrum (b).

RCB could be estimated by subtracting the binding energies at the cutoff point from the photon energies. Here we use the spectra of $[Fe_4Se_4Cl_4]^{2-}$ as an example (Figure 10). The B band was strong in the 266 nm spectrum (Figure 10b), but disappeared completely in the 355-nm spectrum (Figure 10a), indicating that the 355-nm photon (3.496 eV) lies below and the 266 nm (4.661

eV) lies above the top of the RCB corresponding to this detachment channel. Thus, the RCB must be larger than ∼1.1 eV ($h\nu$ − VDE of the B state, i.e., 3.5−2.2 eV) and less than ∼2.5 eV (4.661−2.2 eV). The strong X feature in the 355 nm spectrum also suggested the RCB is less than 2.5 eV (3.5−1.0 eV). The relatively weak A band and its apparent shift to lower binding energy indicated that the higher binding energy part of this band was cut off by the RCB. On the basis of the relative intensities between the A and X band, we estimated that the cutoff point was around 1.5 eV, implying a RCB of ∼2.0 eV (3.5−1.5 eV). This value is in the range bracketed above and is consistent with the cutoff in the 193 and 157 nm spectra (Figure 10c,d). Therefore, we concluded that the RCB of $[Fe_4Se_4Cl_4]^{2-}$ should be around ∼2.0 eV. Similarly, we estimated the RCBs for all the dianions from the photon-energy-dependent PES spectra, as given in Table 1. We noticed that the RCBs of the three halide complexes decrease from $[Fe_4S_4Cl_4]^{2-}$ to $[Fe_4S_4I_4]^{2-}$ due to the increasing physical size, i.e., the increasing Fe-halide bond lengths. The RCBs of the two $[Fe_4Se_4L_4]^{2-}$ species are identical to those of their S counterparts.

PES Spectra and Electronic Structures. The most striking feature in all the PES spectra shown in Figures 2 and 3 is the weak threshold peak X regardless of the ligand type, suggesting that it should have the same origin in all the seven species. This feature, corresponding to removal of the most loosely bound electron, implies that the HOMOs of all the $[Fe_4S_4L_4]^{2-}$ complexes are the same. In our previous PES study of [1Fe] Fe−S complex,[35,42] we observed a similar threshold feature present in all the ferrous Fe(II)-complexes, but not in the ferric Fe(III)-complexes. This band was assigned to removal of the Fe 3d minority spin electron, i.e., $Fe^{II} \rightarrow Fe^{III}$. The similar observation in the PES spectra of $[Fe_4S_4L_4]^{2-}$ and $[Fe_4Se_4L_4]^{2-}$ dianions suggest that the HOMOs of the [4Fe4S] or [4Fe4Se] complexes may have the same character as those of the [1Fe] ferrous complexes because the [4Fe] complexes all contain two ferrous centers formally. This observation is consistent with the MO levels from broken symmetry DFT calculations, which showed that the HOMOs of the $[Fe_4S_4]^{2+}$ core contain two degenerate Fe 3d minority spin levels each from one $[Fe_2S_2]$

(a) **(b)**

Figure 13. Molecular orbital pictures of (a) LUMO and (b) HOMO of $[Fe_4S_4(SCH_3)_4]^{2-}$, and schematic molecular orbital correlation diagrams.

Table 2. B3LYP/6-31G** and Experimental Iron−Iron Distances (Å) and Iron−Sulfur Bond Lengths (Å)

	$[Fe_4S_4(SR)_4]^{3-}$		$[Fe_4S_4(SR)_4]^{2-}$		$[Fe_4S_4(SR)_4]^{1-}$	
	cal.[a]	exp.[b]	cal.	exp.[c]	cal.	exp.[d]
$Fe_{red}-Fe_{red}$	3.234	2.722	2.811	2.716	2.779	2.725
$Fe_{oxd}-Fe_{oxd}$	2.749	2.709	2.811	2.716	3.121	2.754
$Fe_{red}-Fe_{oxd}$	2.954	2.738	2.943	2.724	2.945	2.739
$Fe_{red}-S^*_{red}$	2.469	2.327	2.361	2.263	2.367	2.279
$Fe_{oxd}-S^*_{oxd}$	2.373	2.299	2.361	2.263	2.368	2.271
$Fe_{red}-S^*_{oxd}$	2.402	2.272	2.355	2.303	2.352	2.232
$Fe_{oxd}-S^*_{red}$	2.325	2.269	2.355	2.303	2.267	2.236
$Fe_{red}-S_{red}$	2.355	2.293	2.312	2.259	2.260	2.204
$Fe_{oxd}-S_{oxd}$	2.392	2.306	2.312	2.259	2.244	2.209

[a] R = CH_3. [b] R = Ph ref 54. [c] R = Ph ref 55. [d] R = Ph ref 56.

sublayer. The *X* band corresponds to ionization from the minority spin levels, as schematically shown in Figure 12b for the $[Fe_4S_4Cl_4]^{2-}$ complex.

The second photoelectron band *A* also shows some similarity in all the complexes (Figures 2 and 3). Even the *A*−*X* energy gap (0.75 eV) is identical for all the $[Fe_4S_4L_4]^{2-}$ complexes except for $[Fe_4S_4I_4]^{2-}$, which has a slightly smaller *A*−*X* gap (0.68 eV). The *A*−*X* energy gap in the two Se-cubane complexes (Figure 3) is also identical (0.69 eV) with a slightly smaller magnitude than that of their S-counterparts. However, the relative intensity of the *A* band increased in the spectra of the two $[Fe_4Se_4L_4]^{2-}$ species. This dependence of band *A* on the bridge ligands (S or Se) is consistent with the electronic structure of the [4Fe−4S] cubane from the broken symmetry DFT calculations (Figure 12a). The valence electronic configuration of each [2Fe−2S] sublayer is $[(\sigma_{Fe-S})^{\alpha\beta}(\sigma_{Fe-S^*})^{\alpha\beta}(\sigma^*_{Fe-S})^{\alpha}$-$(\sigma^*_{Fe-S^*})^{\alpha}(\sigma^*_{Fe-S})^{\beta}(\sigma^*_{Fe-S^*})^{0}]$. The HOMO-1 $[(\sigma^*_{Fe-S^*})^{\alpha}]$, which corresponds to the *A* band, is a σ antibonding orbital between Fe and the bridge ligand with mainly ligand characters. The stronger σ donor Se* in the [4Fe-4Se] complex increases the energy level of this orbital and thus decreases the *X*−*A* energy gap. Furthermore, the ionization cross section is expected to be higher for the Se-dominated MO, consistent with the enhanced intensity of the *A* band in the Se-cubane complexes. The $[Fe_4S_4I_4]^{2-}$ complex is special because of the large and soft terminal ligand I^-. Its electron distribution is more diffused, influencing the HOMO-1 orbital and reducing the *A*−*X* energy separation in $[Fe_4S_4I_4]^{2-}$.

Therefore, the current PES data directly show the metal character of the HOMO and the bridge ligand character of the HOMO-1 in the [4Fe] cubane complexes. The higher binding energy features up to 5 eV in Figure 2 change with the different terminal ligands. This part of the spectra are due to the ionization from bonding and antibonding MOs of Fe−S and Fe−S*, S lone pairs, and other ligand-based MOs (Figure 12). The halide features were easily recognizable in the four halide-coordinated cubanes (Figures 2 and 3). The Fe 3*d* majority spin electrons possess too high binding energies to be clearly observed at 193 nm. The higher binding energy tails in the 157 nm data (Figures 4-10) may contain detachment from the Fe 3*d* majority spin electrons, as schematically shown in Figure 12.

The substantial energy gap between the threshold feature *X* and the second ionization band *A* indicates the stability of the high spin d^5 electron configuration in Fe(III)-complexes and provide direct electronic structural basis for the fact that the $[4Fe-4S]^{2+}$ cubane core is used as a reducing agent in HiPIPs or other Fe−S proteins.

The current PES data also provide a direct experimental confirmation for the inverted level scheme and the broken-symmetry DFT description of the electronic structure and spin-couplings of the cubane [4Fe−4S] core (Figure 12). The similarity among the PES data of all the complexes confirms the robustness of the $[4Fe-4S]^{2+}$ core as a modular unit[2] and demonstrates that PES is capable of probing its intrinsic electronic structure.

ADEs, Intrinsic Redox Potentials, and Oxidation Reorganization Energies. A one-electron oxidation reaction, aside from solvation effects, is similar to electron detachment in the gas phase. Therefore, the gas phase ADEs should be inherently related to oxidation potentials, except that the solvation effects are absent in the electron detachment in a vacuum. As discussed above, the threshold feature *X* in the PES spectrum of $[Fe_4S_4L_4]^{2-}$ complex corresponds to removing a minority spin 3d electron from the HOMO of each species. This detachment process represents an oxidation of the [4Fe−4S] core: $[4Fe-4S]^{2+} \rightarrow [4Fe-4S]^{3+}$. The ADE of the *X* band thus represents the gas-phase oxidation potential of the $[Fe_4S_4L_4]^{2-}$ complexes. Consequently, the width of the *X* feature directly reflects the geometry changes after one electron is transferred, and hence is related to the intrinsic reorganization energy (λ_{oxd})

upon oxidization of $[Fe_4S_4L_4]^{2-}$.[35,68,69] The VDE and ADE differences, which characterize λ_{oxd},[35] of all the complexes are listed in Table 1. The λ_{oxd} value is identical for all the seven cubane complexes within our experimental uncertainties, again implying that the $[4Fe-4S]^{2+}$ core is identical regardless of the ligand type or the Se-substitution and further confirming its robustness as a modular unit.[2] Our measured λ_{oxd} value (0.23 eV) for the cubane complexes is in good agreement with a previous calculation [18.3 kJ/mol (0.19 eV)].[68]

Ligand Effects on the ADEs and Redox Potentials. As shown in Table 1 and Figures 2 and 3, the ADEs of the cubane complexes are largely influenced by the terminal ligand but not sensitive to the bridging S* or Se*. The strong electron donor ligands, $-SC_2H_5$ and $-SH$, yield much lower ADEs than the electron withdrawing halide ligands, suggesting that the HOMO of $[Fe_4S_4L_4]^{2-}$ has considerable contribution from the ligand orbitals, in addition to the Fe $3d$ character. As shown in Figure 13, the HOMO of $[Fe_4S_4(SCH_3)_4]^{2-}$ arises from the interaction between the high-lying occupied minority-spin Fe(3d) orbitals and the terminal ligand lone pairs, Lp(S). Raising the energy of Lp(S) causes the energy gap between the Lp and the Fe d_{Fe-Fe} set to diminish and enhances the interaction between the ligand and Fe. This would destabilize the σ^*_{Fe-S} orbital, resulting in a decrease of the oxidation energy. Thus, the terminal thiolate ligands, which are strong σ donors, decrease the ADE and VDE of $[Fe_4S_4(SCH_3)_4]^{2-}$ and make it easy to be oxidized.

However, the substitution of the bridging S* by Se* in $[Fe_4Se^*_4(SR)_4]^{2-}$ has little effect on the ADE and VDE, compared to the S counterparts (Figure 3). This is consistent with the nature of the σ^*_{Fe-S} orbital, which has little contribution from the bridging S* (Figure 13).

On the other hand, the LUMO of $[Fe_4S_4(SCH_3)_4]^{2-}$ arises from the interaction between the minority-spin Fe(3d) orbitals and the bridging ligand lone pairs, Lp(S*) (Figure 13). The bridging Se* substitution in $[Fe_4Se^*_4(SR)_4]^{2-}$ leads to an increase in energy of the $\sigma^*_{Fe-Se^*}$ orbital (LUMO) and a decrease in energy of the σ_{Fe-Se^*} orbital. Thus, the redox potential of the $[Fe_4S_4L_4]^{3-}/[Fe_4S_4L_4]^{2-}$ couple mainly depends on the electron donor tendency of the bridging ligands.

Conclusions

We report a study on the electronic structure of a series of $[4Fe-4S]$ cubane complexes, $[Fe_4S_4L_4]^{2-}$ (L = SH, SC_2H_5, Cl,

Br, I) and the Se-substituted species $[Fe_4Se_4L_4]^{2-}$ (L = Cl, SC_2H_5) in the gas phase using photoelectron spectroscopy and broken-symmetry density functional calculations. Photoelectron spectra were obtained at several photon energies, allowing characterization of the repulsive Coulomb barriers and intramolecular Coulomb repulsion in these doubly charged anions. All the seven cubane complexes exhibit similar spectral features, showing the robustness of the $[4Fe-4S]$ cluster as a modular unit. A weak threshold peak was observed in all the spectra due to ionization of the Fe 3d minority electrons. Spectral features due to the bridging ligands and the terminal ligands were also observed at higher electron binding energies. The spectral features confirm the low-spin two-layer model for the $[4Fe-4S]^{2+}$ core and its "inverted level scheme" molecular orbital diagrams. We found the ADEs, which provide the intrinsic oxidation potentials of the $[Fe_4S_4L_4]^{2-}$ complexes, are very sensitive to the terminal ligands, but independent of the substitution of the inorganic S by Se. The DFT calculations revealed that the HOMO of $[Fe_4S_4L_4]^{2-}$ is derived from the interaction of the Fe 3d minority spin−orbitals and the ligand lone pair electrons and that the HOMO energy depends on the electron donor property of the terminal ligands consistent with the experimental observation of the variation of the ADEs with the terminal ligands. The LUMO of $[Fe_4S_4L_4]^{2-}$ is derived from the interaction of the Fe 3d minority spin−orbitals and the inorganic S (bridging) lone pairs. Thus, the reduction energy of $[Fe_4S_4L_4]^{2-}$ should be sensitive to the donor property of the bridging S* or Se* substitution. The current study provides a molecular basis for deconvoluting the factors that control the redox properties of the proteins, such as the effects of solvent, hydrogen-bonding, and electrostatic potentials induced by local charge groups or protein mutations, which is the focus of future studies.

(68) Sigfridsson, E.; Olsson, M. H. M.; Ryde, U. *Inorg. Chem.* **2001**, *40*, 2509.
(69) Sigfridsson, E.; Olsson, M. H. M.; Ryde, U. *J. Phys. Chem. B* **2001**, *105*, 5546.

JA036831X